1

Crystallography and Mechanical Properties of Intercritically Annealed Quench and Partitioned High-Aluminum Steel

T. Nyyssönen[a,e], P. Peura[b], E. De Moor[c], D. Williamson[e], V.-T. Kuokkala[b]

[a]*Outotec Oyj, Kuparitie 10, 28330 Pori, Finland*
[b]*Laboratory of Materials Science, Tampere Univ. of Technology, P.O. Box 589, 33101 Tampere, Finland*
[c]*Advanced Steel Processing and Products Research Center, Colorado School of Mines, 1500 Illinois Street, Golden, CO 80401, USA*
[d]*Department of Physics, Colorado School of Mines, 1523 Illinois Street, Golden, CO 80401, USA*
[e]*Corresponding author. E-mail: tuomo.nyyssonen@outotec.com, tel: +358503721641*

Abstract

The quenching and partitioning response of intercritically annealed steel with aluminum contents in the 2-3 wt.% range and a carbon content of 0.2 wt.% was studied. Two types of morphologies for retained austenite were observed in electron backscatter diffraction studies: blocky, untransformed austenite grains and partially transformed austenite located primarily at prior austenite and packet boundaries. The amount of retained austenite was found to correlate with the initial quench temperature, as well as with the uniform elongation of the specimens in subsequent tensile testing. The transformation characteristics of austenite were rationalized on the basis of prior austenite grain size and inhomogeneous carbon distribution. The martensite transformed during the initial quench was found to favor $\Sigma 3$ twin-type lath combinations, supplemented by neighboring variants providing self-accommodation.

Keywords: `phase transformation, quenching, partitioning, EBSD, steel`

1. Introduction

Quenching and partitioning has been shown to produce excellent mechanical properties for silicon-alloyed steels quenched from a fully austenitized condition [1]. However, the necessity to quench the steel from a fully austenitized state to an intermediate quench temperature (in the 200-350 °C range) requires significant adjustments to existing annealing lines to accurately obtain these temperatures. In addition, silicon makes hot dip galvanization a difficult procedure, precluding the use of these alloys in applications where corrosion protection is a necessity [2]. This is a big hindrance, considering that the major target application for high-strength steels is the automotive industry. Finally, new production methods and structural designs are required to fully take advantage of the enhanced properties.

A logical step on the way to adopting quenched and partitioned microstructures would be the development of an intermediate-level grade in terms of strength, galvanizable with the current level of technology, which would still benefit from the increased formability resulting from the Q&P treatment. A dual-phase steel with a quenched and partitioned microstructure replacing the martensitic phase would fulfill these requirements. Aluminum is an alloying element that has frequently been used to achieve the same effect as silicon in TRIP steels, and it has been shown to allow for hot dip galvanizing [2].

In this work, we conducted quenching and partitioning experiments, combined with intercritical annealing, on two high-aluminum TRIP-type steels with a nominal carbon content of 0.2 wt-% and aluminum content in the 2-3 wt.% range. The focus was on the morphology and transformation characteristics of the martensite and intercritical austenite investigated primarily through elec-

tron backscatter diffraction (hereafter EBSD). Additionally, the partitioning of carbon from martensite to austenite was investigated through x-ray diffraction (hereafter XRD) and Mössbauer measurements at a range of partitioning times. The mechanical properties of the steels were investigated through tensile testing.

2. Martensite transformation from intercritical austenite

The model used by Speer et al. [3] to explain the microstructural evolution of steel during quenching and partitioning can be used to obtain a prediction for the maximum amount of retained austenite (and corresponding quench temperature T_{iq}) for a given alloy composition. This estimate is largely based on the amount of carbon needed to lower the martensite start temperature M_s of retained austenite to just below room temperature, according to the particular equation or method selected for calculating M_s for a given steel composition. The carbon for stabilizing the retained austenite is assumed to diffuse from supersaturated martensite formed during a partial martensitic transformation that has been interrupted by quenching to a temperature T_{iq}, which is necessarily above the martensite transformation finish temperature M_f. This diffusion of carbon from martensite to austenite is referred to as partitioning and is performed either at T_{iq} or at a slightly elevated temperature T_p. The assumption is that carbide precipitation is suppressed or delayed during partitioning by suitable alloying elements. Ideally, the resulting microstructure consists of carbon-rich retained austenite in a carbon-free martensitic matrix.

From a Q&P perspective, an intercritical annealing temperature between Ac_1 and Ac_3 opens up some interesting heat treatment design possibilities. By selecting the annealing temperature to produce a smaller fraction of intercritical

4

austenite, the austenite alloying composition corresponding to thermodynamic equilibrium changes and most notably the carbon content of the austenitic phase increases. Thus by carefully selecting the intercritical annealing temperature, the M_s temperature of the selected alloy can be modified and the optimal quench temperature can be controlled, which may be desirable from a production point of view.

For binary alloys, the chemical composition of the phases at an intercritical equilibrium can be readily obtained from phase diagrams by using the lever rule. In the case of multicomponent alloys, it is a common practice to use a suitable thermodynamic database, such as JMATPRO® [4]. A phase fraction-temperature diagram can be constructed to predict the phase fractions and compositions for a desired range of intercritical annealing temperatures. The basic Q&P methodology can be used in combination with this information to gain an idea of the potentially available microstructures and properties.

An example calculation for a hypothetical intercritically annealed steel with the composition Fe-0.2C-2Mn-2Al (wt.%) is shown in Figure 1. The phase fractions and compositions were calculated for the steel alloy using JMATPRO® [4], at a temperature range of 750-900 °C with 10 °C intervals. For each annealing temperature interval, the composition of the austenite phase was used to calculate the quench temperature resulting in maximum retained austenite according to the methodology by Speer et al. [3]. The M_s temperatures were calculated based on the semi-empirical method proposed by Bhadeshia [5, 6] that balances the calculated available driving force for martensitic transformation against the chemical free energy change accompanying the transformation from austenite to martensite, taken as an empirically determined linear rela-

5

tionship depending only on carbon content. Substitutional alloying elements are taken into account by allowing for their effects on the magnetic and non-magnetic components of the transformation free energy change, as well as the effect on carbon-carbon interaction energy. The Koistinen-Marburger equation, modified by Van Bohemen-Sietsma's kinetic equations [7, 8], was used to calculate the extent of the martensitic transformation with respect to temperature:

$$V_m = 1 - e^{(-k(M_s - T))} \tag{1}$$

In Equation 1, T is the temperature in K, M_s is the temperature of the onset of martensitic transformation in K and k is an empirically determined variable. The effect of chemical composition on k was determined by van Bohemen and Sietsma to follow Equation 2:

$$k^{-1} = 0.0224 - 0.0107C - 0.0007Mn - 0.00005Ni - 0.00012Cr - 0.0001Mo \tag{2}$$

The amount of each alloying element in Equation 2 is in wt-%. The Equation indicates that increasing carbon content strongly decreases the rate of the martensitic transformation with respect to temperature.

Figure 1a) shows that the choice of intercritical annealing temperature has a significant effect on the balance of phases after final quenching, primarily affecting the balance of ferrite and martensite. A lower intercritical annealing temperature results in a lower optimal T_{iq}, as well as a reduced amount of martensite in the final microstructure. The equilibrium composition for the intercritical austenite phase is shown in Figure 1b). In effect, full partitioning
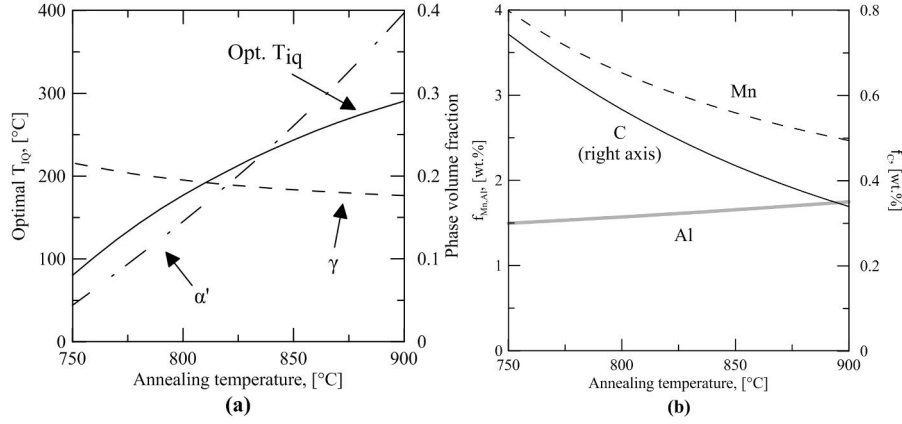
6

Figure 1: Calculations with Speer's method for modeling the optimal Q&P quench temperature for various intercritical austenite fractions and chemical compositions (modeled with JMATPRO® [4]). Figure 1a) shows the calculated T_{iq} resulting in a maximum amount of retained austenite, as well as the maximum retained austenite content and corresponding martensite fraction with respect to annealing temperature. Figure 1b) shows the equilibrium composition of the intercritical austenite phase.

of all elements dictated by thermodynamic equilibrium is assumed to have occurred between the phases. This state is assumed to be maintained until the conclusion of the initial cooling step to T_{iq}. It should be noted that the austenite fraction corresponding to the composition at each temperature in Figure 1b) can be extracted from Figure 1a) by the addition $\alpha' + \gamma$.

In Figure 1a), the quench temperature resulting in maximum retained austenite is calculated on the assumption that the steel alloy has reached thermodynamic phase and compositional equilibrium. Achieving this state will take time, however, determined by the kinetics of austenite nucleation and growth. It was shown by Garcia et al. [9] that for a 0.22C-1.5Mn steel with a cold rolled starting microstructure, it took approximately ten hours to achieve thermodynamic equilibrium of 42 vol.% austenite when annealing at 725 °C. This type of slow growth has been attributed to the slow rate of substitutional diffusion of heavier alloying elements (such as Mn or Cr) [9, 10, 11], which becomes the controlling

7

factor at temperatures close to Ac_1.

Aluminum is an alloying element that raises Ac_1 and Ac_3 temperatures significantly [12]. This is shown by Figure 1, in which thermodynamic equilibrium at 850 °C corresponds to nearly 44 vol.% of austenite. A prior study by some of the present authors [13] showed that for this approximate composition (Steel A in Table 1), the observed austenite volume fraction after 3 minutes of annealing at 850 °C was approximately 29 vol.%, rising to 35 vol.% when annealing time was increased to 1 hour. These results suggest that aluminum additions at a range of 2-3 wt.% have a significant slowing effect on austenite growth kinetics. For comparison, it has been shown that full austenitization takes 3 minutes for a 0.22C-1.5Mn steel [9] at 850 °C.

Additionally, it was observed in the prior study [13] that austenite grain size remains very small in the intercritical condition for high-aluminum steels. Representative micrographs are shown in Figure 2. After three minutes of annealing, austenite grain size (reported as area weighted point-sampled intercept length) was on the order of 1 μm with a standard deviation of approximately 0.5 μm, with a slight increase to approximately 1.5 μm with 1 μm standard deviation after annealing for one hour. Figure 3 shows a prediction for the distribution of undercooling to M_s using the model proposed by Yang and Bhadeshia [14] for an M_s grain size correction. The Figure shows the results as a normalized histogram, along with a fit for a gaussian standard deviation function.

It was shown [13] that by correcting the M_s calculation to account for the observed phase fractions and grain sizes the calculated M_s value becomes close to the experimentally observed value. Thus, the deviation between the observed
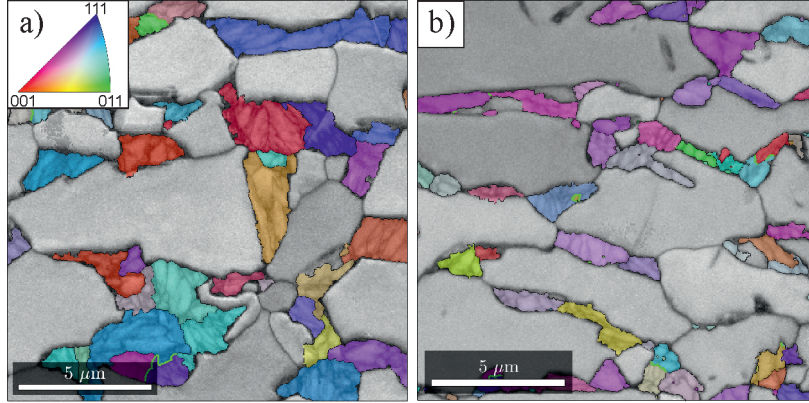
8

Figure 2: The effects of intercritical annealing for Steel A (refer to Table 1) at 850 °C for a) 1 hr and b) 3 minutes, shown on EBSD band contrast images overlaid with reconstructed austenite grain map colored with IPF TD coloring (see a) for color key). The maps represent 15×15 μm areas measured at a step size of 0.05 μm. Regarding references to color, see the online version of the article.

low M_s values and the high predicted values is clearly related to the slow austenite growth kinetics and the small austenite grain sizes in the initial prediction. The evidence suggests that high aluminum contents slow down austenite formation kinetics at temperatures where leaner steel alloy compositions (such as those studied by Garcia et al. [9]) would have quickly reached equilibrium. The kinetics of austenite formation and growth must therefore be taken into account to determine Q&P processing parameters.

Based on Figure 3, quenching to a temperature T_{iq} will in practice likely not result in a uniform martensitic transformation in the material, even if the grains are chemically homogenous. More likely, the resulting microstructure will consist of prior austenite grains that have each undergone a martensitic transformation to a degree specified in part by their grain size, as well as chemical composition. It was observed by Jimenez-Melero et al. [15] in synchrotron studies for high-aluminum TRIP steels that significant variation exists in the carbon concentration and grain size from grain to grain. In their studies, the
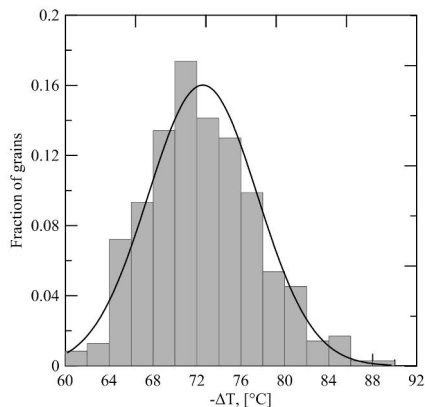
9

Figure 3: Histogram describing the calculated additional undercooling ΔT to M_s caused by prior austenite grain size for a steel with a measured M_s of 170 °C and a grain size distribution of approximately 1.5 μm $\pm$ 1 μm . Calculated with the equation proposed by Yang and Bhadeshia [14] using the measured grain size and M_s data from prior work [13].

carbon contents in individual austenite grains ranged from 0.8 to 1.4 wt.% in a TRIP steel with composition Fe-0.2C-1.5Mn-1.8Al-0.37Si (wt.%). It is therefore probable that when quenching an intercritically annealed high-aluminum steel to a specific T_{iq}, some austenite grains are transformed to a very limited degree while others may have undergone a full or nearly full martensitic transformation.

An example calculation for a hypothetical 0.2C-2Mn-2Al (wt.%) composition is shown in Figure 4. It is assumed that the intercritical annealing has resulted in a 25 vol.% austenite fraction. All of the carbon is assumed to have fully partitioned into the austenite during annealing, giving an average austenite carbon content of 0.8 wt.%. The average austenite grain size is assumed to be $L_{avg} = 1.5$ μm, resulting in $M_s = 130$ °C using Bhadeshia's method and the grain size correction by Yang et al. [14] The austenite grains are assumed to have a size distribution that allows the existence of two grains of size $L_1 = 2$ μm and $L_2 = 1.5$ μm. The carbon contents are assumed to be $C_{\gamma 1} = 0.7$ wt.% for the large grain and $C_{\gamma 2} = 0.8$ wt.% for the small. Both grain sizes and carbon
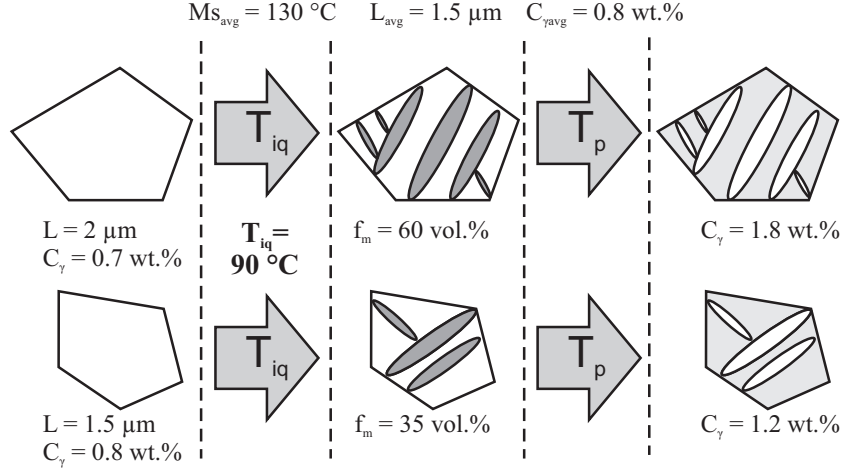
10

Figure 4: A schematic describing the degree of martensitic transformation at a specific T_{iq}, as well as the final carbon content after partitioning for two austenite grains with a varying size and carbon content.

contents are well within the distributions observed in previous studies [15, 16]. The intercritically annealed steel is subjected to a quenching and partitioning treatment with $T_{iq} = 90°C$, followed by full partitioning. M_s is then recalculated for grains 1 and 2 and the extent of the martensitic transformation at $T_{iq} = 90°C$ is determined separately using the Koistinen-Marburger equation. Figure 4 shows that for the large, low-carbon grain, the martensite fraction f_m reaches 60 vol.% during the initial quench, while the smaller grain transforms only to the extent of 35 vol.%. Assuming full partitioning, this results in a 1.8 wt.% carbon content for the larger grain and 1.2 wt.% for the small grain. The extent of martensitic transformation during the initial quench and the consequent potential austenite stability is completely different for the grains. The situation is further complicated by the fact that (following a similar calculation) grains below the size of 1 μm and with carbon contents above 0.85 wt.% will not transform at all during the initial quench.

Based on the calculations, it is probably not practical to seek a homoge-

nous partial transformation of the austenitic phase after intercritical annealing within industrially relevant timeframes. It is more likely that in practice, after quenching to a specific T_{iq}, some austenite grains are transformed to a very limited degree while others undergo a nearly full martensitic transformation. The large grains with low carbon contents will transform to a greater degree than small grains with high carbon contents. It follows that the austenite grains that have undergone a larger degree of transformation will have a greater individual volume fraction of carbon-supersaturated martensite from which to partition carbon into the remaining austenite.

The resulting microstructure of a quenched and partitioned intercritically annealed steel could then be considered to share certain microstructural aspects with TRIP (untransformed, small-sized blocky austenite) and DP (islands of martensite with a small amount of high-stability retained austenite) steels. The aim of the experimental section in this study was to determine the heat treatment parameters to produce this kind of microstructure for high-aluminum steels, as well as characterize the resulting microstructure, crystallography and mechanical properties to a relevant degree.

3. Materials and Methods

Two high-aluminum steels with a nominal carbon content of 0.2 wt.% were prepared for the studies (hereafter referred to as steels A and B). The steel compositions are shown in Table 1. Approximately 1 wt.% of Cu and 0.5 wt.% of Ni were added to the composition of Steel B to offset the increase in Ac_3 caused by the high aluminum content. The alloys were vacuum-cast as $40 \times 40 \times 180$ mm billets into a water-cooled copper die. The specimens were annealed at 1200 °C for 30 minutes prior to hot rolling in a laboratory rolling mill. The samples

were hot rolled into 3 mm sheets with the finishing rolling temperature at 900 °C, quenched to 600 °C and insulated to cool slowly overnight, thus simulating the cooldown after coiling. The samples were then cold rolled into 60 mm wide, 1.3 mm thick strips, from which 10×60 mm heat treatment specimens were cut.

The specimens were then subjected to quenching and partitioning treatments. A thermocouple was attached to each specimen and the temperature was monitored to ensure the validity of the heat treatment cycle and to determine the cooling and heating rates. The specimens were held in a laboratory tube furnace and heated at an average heating rate of approximately 4 °C/s to 850 °C, followed by a 4 minute soak. They were then immersed into a heated oil bath, allowed to cool at an average cooling rate of 25 °C/s and held at T_{iq} for 10 seconds. This was followed by partitioning by immersing the specimen into a molten salt bath at 450 °C, corresponding to an average heating rate of approximately 25 °C/s followed by holding for the given partitioning time. The heat treatment parameters for the steels are listed in Table 2. Three specimens were prepared for each heat treatment condition: one for microstructural characterization via x-ray diffraction (hereafter XRD) and EBSD, two for tensile testing.

Tensile testing was carried out using an Instron 8800 servohydraulic materials testing machine. Non-standard tensile specimens were prepared by precision milling a 6 mm long, 3.5 mm wide gage area into the centre of each specimen.

Table 1: Chemical compositions of the investigated steels.

Element [wt.%]	C	Mn	Si	Al	P	Ni	Cu	Nb	Cr
Steel A	0.19	1.99	0.38	1.96	0.05	0.02	0.02	0.03	0.11
Steel B	0.22	2.03	0.04	2.93	0.01	0.48	0.96	0.03	0.12

Table 2: The heat treatment parameters of the tested specimens.

Steel	T_q, [°C]	T_p, [°C]	t_p, [s]
A	100	450	10
			100
			1000
	125	450	10
			100
			1000
B	50	450	10
			100
			1000
	75	450	10
			100
			1000
	100	450	10
			100
			1000

241   Each specimen was tested in tension to fracture at a strain rate of 0.001 s-1.

242

243   The specimens were prepared for x-ray diffraction by grinding with P800
244   silicon carbide paper to remove 0.2 mm of material from the specimen surface,
245   followed by grinding with progressively finer grit size up to P2000. Finally, the
246   specimens were electrolytically polished with a Struers Lectropol-5 polishing
247   unit for 12 seconds at 40 V using the Struers A2 electrolyte. The XRD analyses
248   were conducted with the Panalytical Empyrean X-Ray diffractometer using Co
249   Kα-radiation and a Fe filter ($48° < 2\theta < 130°$, 40 kV, 45 mA). The peaks used in
250   the analysis were (110), (200), (211) and (220) for martensite and (111), (200),
251   (220) and (311) for austenite. The retained austenite fraction was calculated
252   from the integrated peak intensities using the methodology defined in ASTM E
253   975-95 [17]. The average lattice parameter a_γ was calculated from the austenite
254   peaks and used to calculate the carbon content of austenite with the following
255   equation [15]:

14

256

$$a_\gamma = 3.556 + 0.0453 x_C + 0.00095 x_{Mn} + 0.0056 x_{Al} \qquad (3)$$

257   where a_γ is in Å and x_C, x_{Mn} x_{Al} are in wt.%.

258

259   The EBSD specimens were sectioned from the XRD specimens at the loca-
260   tion of the thermocouple, ground and polished with 0.1 μm colloidal silica used
261   in the final polishing step. EBSD studies were conducted with a Zeiss Ultra
262   Plus UHR FEG-SEM system fitted with a Nordlys F400 EBSD detector, using
263   a 20 kV acceleration voltage, 120 μm aperture, and 14 mm working distance.

264

265   Mössbauer spectroscopy was conducted to obtain information on the effect
266   of partitioning time on austenite carbon content and carbide volume fractions.
267   Salt bath heat treatments were performed to obtain specimens for testing. 18x60
268   mm specimens were cut from the cold rolled sheets and annealed by immersion
269   in a 850 °C salt bath for a holding time of four minutes. The specimens were
270   then immersed in a heated oil bath of temperature T_{iq} = 75°C, after which
271   they were immediately transferred to a 450 °C salt bath for partitioning times
272   of 10 s and 1000 s. The Mössbauer specimens were ground by hand to 0.1
273   mm thickness and then immersed in a chemical polishing solution of 10:10:1 de-
274   ionized water:hydrogen peroxide (70% water:30% H2O2):hydrofluoric acid (52%
275   water: 48% hydrofluoric acid) until they had thinned to approximately 30 μm
276   thickness. The measurements were carried out in the manner described in [18],
277   using the same spectrometer.

15

4. Results

Figure 5 shows the combined results for yield strength, ultimate tensile strength (UTS), uniform elongation (Ag), total elongation and retained austenite contents for Steels A and B with respect to the initial quench temperature T_{iq}. There was no significant variation in the austenite carbon content of the steels determined with XRD. Both steels had a carbon content of approximately 1.15-1.2 wt.% regardless of T_{iq}. It should be noted that the carbon contents were calculated with Equation 4 using the average chemical composition of the steels.

In Figure 5, the total elongation ε_{tot} has been calculated to correspond to standard test geometry of 120 mm x 20 mm gage section using the Oliver equation as implemented by ISO 2566/1 [19]:

$$A_2 = A_1 \times (\frac{k_1}{k_2})^n \tag{4}$$

where A_2 is the calculated elongation value, A_1 is the known elongation value, k_1 and k_2 are the proportionality ratios of the two test pieces, and n is a material dependent constant. The standard adopts $n = 0.4$.

T_{iq} is found to correlate with the fraction of retained austenite, as well as uniform elongation Ag and total elongation ε_{tot}. T_{iq} appears to have an inverse correlation with the yield point Rp_{05} and ultimate tensile strength.

Examples of the stress-strain curves are shown in Figure 6 for both Steels at all quench temperatures and with the partitioning time of 100 s. There was no appreciable change in the shape of the curves with increased or decreased partitioning time. Figure 6b) shows that increasing T_{iq} clearly increases the amount of work hardening in Steel B, as well as the ductility. The effect of T_{iq} on work
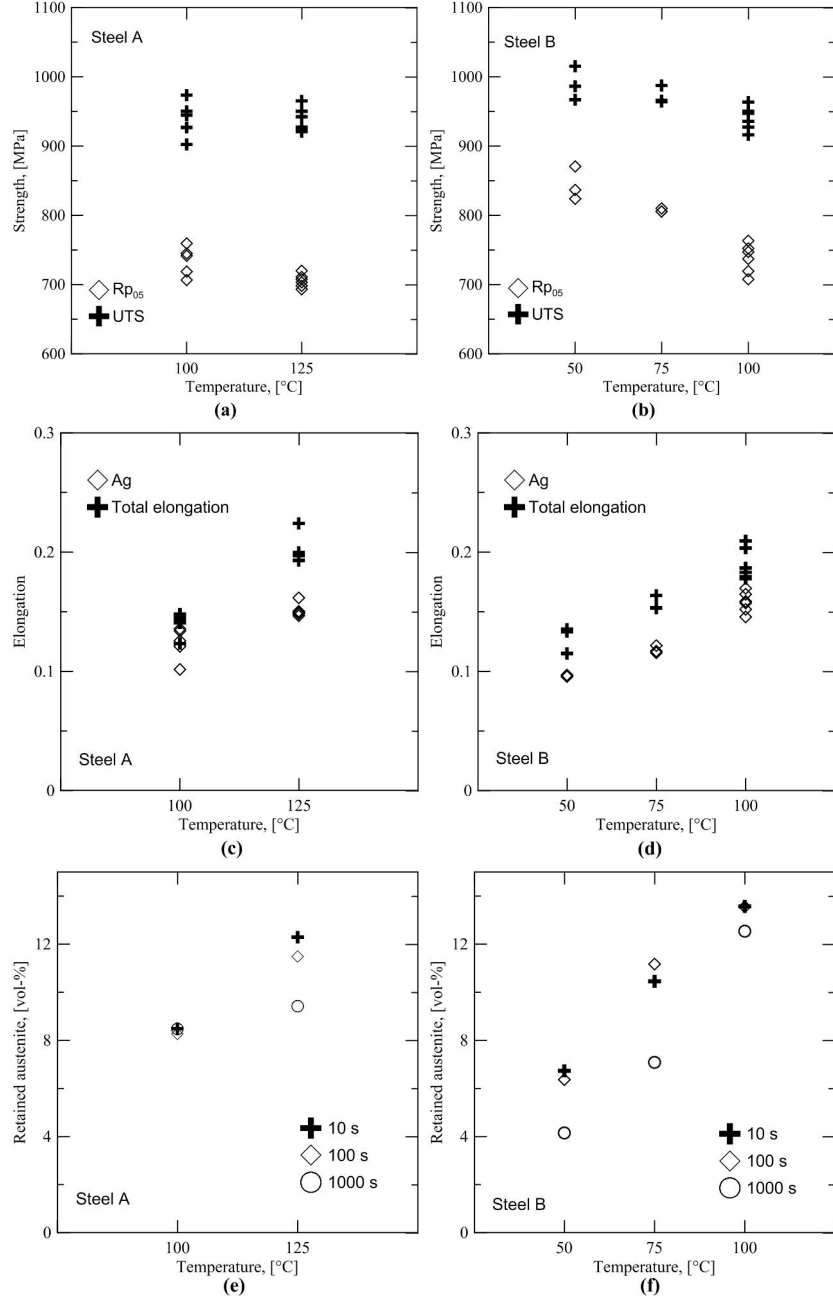
16

Figure 5: Yield point Rp_{05} and ultimate tensile strength UTS (a and b), uniform elongation Ag and total elongation (c and d) and retained austenite contents (e and f) for Steel A (a, c, e) and Steel B (b, d, f), with respect to T_{iq}.
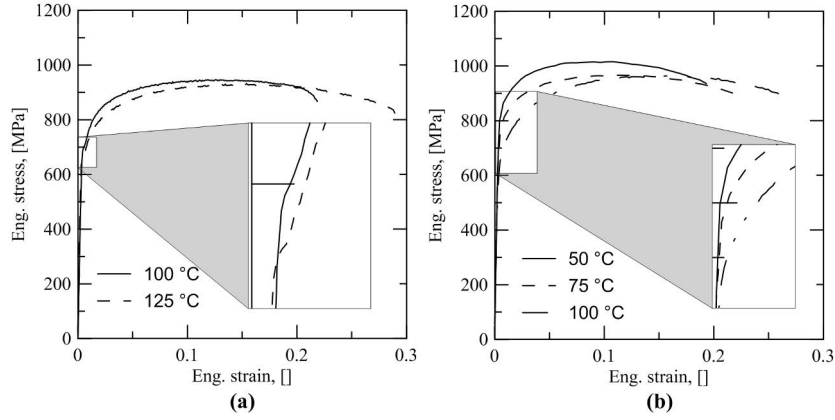
17

Figure 6: Engineering stress-strain curves for a) Steel A and b) Steel B. T_{iq} is indicated in the legend. The elongation after necking is uncorrected (compare to Figure 5).

hardening is much smaller in the case of Steel A, for which work hardening is significant for both quenching temperatures. At $T_{iq} = 100$ °C, steel B exhibits a similar degree of hardening to steel A. A knee in the yield point can also be observed in the stress-strain curve of steel A, as indicated in the enlarged view in Figure 6a).

Figure 7 shows EBSD band contrast images for the steels. For both steels, the microstructure consists of intercritical ferrite and austenite that has partially transformed to martensite. The prior austenite grains in Figure 7a) and c) can be divided into untransformed, partially transformed and completely transformed categories. Figures 7b) and 7d) show examples of sub-micron retained austenite grains intermixed with martensite that clearly originate from the same prior austenite grain.

The Mössbauer specimens exhibited similar behavior with regards to retained austenite content. The low amount of carbides present in the microstructure of the specimens precluded the resolution of η-carbide and cementite, so
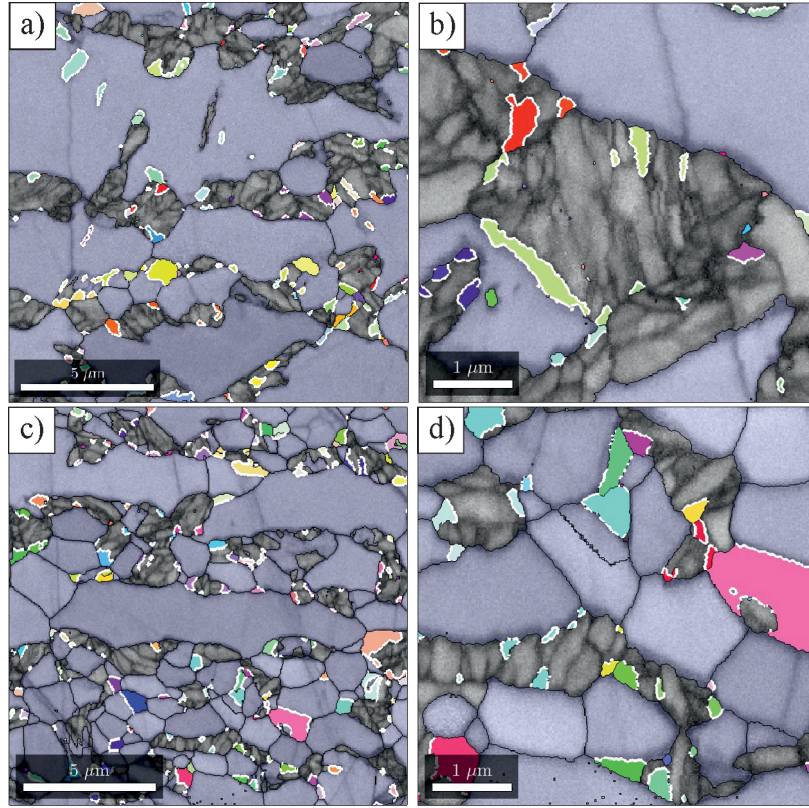
18

Figure 7: EBSD band contrast images overlaid with retained austenite grain map colored with IPF TD coloring (refer to Figure 2a for color key). Phase boundaries corresponding to K-S orientation relationship with 5 degree tolerance indicated with white. Intercritical ferrite grains have been emphasized with blue overlay. The maps represent 15×15 μm areas measured at a step size of 0.05 μm (a,c) and 5×5 μm areas measured at a step size of 0.02 μm (b,d) for Steel A, $T_{iq} = 125°$, $t_P = 100s$ (a,b) and Steel B (c,d), $T_{iq} = 100°$, $t_P = 100s$. Regarding references to color, see the online version of the article.

they are referred to here only as "carbide". After ten seconds of partitioning, Steel A had 10.0 at.% Fe as retained austenite and 0.09 at.% Fe as carbide. After 1000 s of partitioning, the austenite Fe fraction had decreased to 8.0 at.% and the carbide Fe fraction increased to 0.46 at.%. After ten seconds Steel B had a retained austenite Fe fraction of 11.4 at.% and a carbide Fe fraction of 0.25 at.%. After 1000 s, the austenite Fe fraction was measured at 12.5 at.% and the carbide Fe fraction as 0.19 at.%. Also, after 1000 s, Steel B was measured
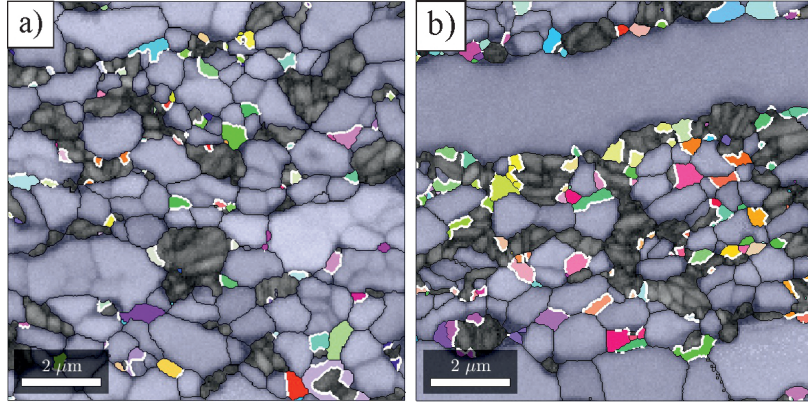
19

Figure 8: EBSD band contrast images overlaid with retained austenite grain map colored with IPF TD coloring (refer to Figure 2a for color key). Phase boundaries corresponding to K-S orientation relationship with 5 degree tolerance indicated with white. Intercritical ferrite grains have been emphasized with blue overlay. The maps represent 10×10 μm areas for a) Steel A and b) Steel B quenched to $T_{iq} = 75$ °C and partitioned at 450 °C for 1000 s. Regarding references to color, see the online version of the article.

to have an austenite carbon content of 5.2 at.% = 1.12 wt.%, in reasonable agreement with the XRD measurements.

The heat treatment cycle of the Mössbauer samples differed significantly from the other samples studied here. Consequently, EBSD measurements were made to ascertain whether the results are comparable from a microstructural point of view. Figure 8 shows the EBSD results. The amount of completely untransformed austenite grains is higher in the samples annealed for this study. It also appears that the intercritical ferrite has not been completely recrystallized during the shorter annealing cycle.

5. Discussion

The observed correlation between T_{iq} and retained austenite content as well as the microstructures shown by Figure 7 indicate that steels A and B have undergone a partial martensitic transformation followed by the stabilization of

the retained austenite during the partitioning step. The correlation of the fraction of retained austenite with Ag and ε_{tot} indicates that the retained austenite contributes to the ductility of the steels. It should be stressed that the sheer amount of retained austenite does not directly improve ductility; rather it is the work hardening caused by the martensitic transformation of this retained austenite during plastic deformation.

It is possible to do some accounting for carbon using the Mössbauer results for Steel B partitioned for 1000 s. The fraction of total carbon in the carbide phase is estimated as 0.1 at.% = 0.02 wt.%, assuming carbide stoichiometry of M_2C. Thus, the carbide amounts to about 10 % of the total carbon in the steel and the austenite accounts for about 70 % of the total carbon, leaving about 20 % of the carbon in solution in the martensite or ferrite phases. These values are comparable to those obtained in a recent study on the quenching and partitioning behavior of steel alloys with the compositions of approximately 0.2C-1.5Mn-1.3Si-1.5Cr-0.07Ni wt.% and 0.2C-1.5Mn-1.3Si-0.01Cr-1.5Ni wt.% [20]. The calculations for the specimens studied in this work indicate that carbide precipitation has been suppressed to a degree for the duration of the partitioning. However, it should be noted that the morphology of the retained austenite in the Mössbauer experiment differed slighty from that of the other specimens. It is possible that some of the carbon remains in the intercritical ferrite phase to form Cottrell atmospheres around dislocations, which would explain the discontinuous yielding observed in Steel A (see Figure 6a). This type of behavior has been observed in dual-phase steels in previous studies [21].

The previously discussed assumption of the heterogeneity of the martensitic transformation appears to hold for the tube furnace-annealed specimens, based

on Figure 7a) and c). Several untransformed austenite grains are apparent in
the grain map. Then again, several larger prior austenite grains have undergone
a partial martensitic transformation, as evidenced by Figures 7b) and d), where
several austenitic orientation pixel clusters are divided by martensitic regions,
yet share the same crystallographic orientation. In addition, this type of retained
austenite and the surrounding martensite share an orientation relationship close
to the Kurdjumov-Sachs [22] OR, which is described by the parallelism of the
$(111)\gamma$ and $(011)\alpha'$ planes and the $[\bar{1}01]\gamma$ and $[\bar{1}\bar{1}1]\alpha'$ directions.

A critical analysis of the degree of transformation in each austenite grain
from the orientation maps is not possible, since the fraction of orientation pixels
indexed as austenite is approximately one fifth of the fraction determined via
XRD. This may be due to some of the austenite having a film-type morphology
too fine to detect with EBSD. It is also possible that some of the austenite has
transformed into martensite during EBSD specimen preparation.

Some general features, however, can be determined for both martensite and
austenite. Three orientation maps of dimensions 35×25 μm at a resolution of
0.05 μm were measured for both steel A quenched to 125 °C and partitioned for
100 s and for steel B quenched to 100 °C and partitioned for 100 s. For these
maps, the lath boundaries were resolved and indexed by using the iterative orientation
relationship determination algorithm described in [16]. Instead of grain
pair misorientations, all of the individual misorientations between neighboring
orientation pixels in the map were used for the orientation relationship determination.
This was done to increase the amount of data available to the algorithm.
Each misorientation was indexed according to the notation used by Morito et
al. [23], in which the first six misorientations correspond to the misorientations

between variants in the same packet. The 24 possible misorientations between

martensitic laths were generated with the iteratively determined orientation re-

lationship for Steel A and are shown in Table 3, following the notation by Morito

et al. [23]

Table 3: 24 variants in martensite as defined by Morito et al. [23]. Misorientation axes and angles are shown for the OR measured for steel A.

| Variant	Plane parallel	Direction parallel	Rotation from Variant 1	
No.		$[\gamma]\|\|[\alpha']$	Axis (indexed by martensite)	Angle [deg.]
V1		$[\bar{1}01]\|\|[\bar{1}\bar{1}1]$	-	-
V2		$[\bar{1}01]\|\|[\bar{1}1\bar{1}]$	[-0.5301 0.5426 0.6516]	60.23
V3	$(111)\gamma$	$[01\bar{1}]\|\|[\bar{1}\bar{1}1]$	[-0.7003 0.0151 0.7137]	60.01
V4	$\|\|(011)\alpha'$	$[01\bar{1}]\|\|[\bar{1}1\bar{1}]$	[-0.6092 0.0000 0.7931]	5.16
V5		$[1\bar{1}0]\|\|[\bar{1}\bar{1}1]$	[-0.0151 0.7003 0.7137]	60.01
V6		$[1\bar{1}0]\|\|[\bar{1}1\bar{1}]$	[-0.7069 0.0223 0.7069]	54.89
V7		$[10\bar{1}]\|\|[\bar{1}\bar{1}1]$	[-0.6050 0.5177 0.6050]	50.73
V8		$[10\bar{1}]\|\|[\bar{1}1\bar{1}]$	[-0.6926 0.2016 0.6926]	10.38
V9	$(1\bar{1}1)\gamma$	$[\bar{1}\bar{1}0]\|\|[\bar{1}\bar{1}1]$	[-0.6560 0.2092 0.7252]	52.30
V10	$\|\|(011)\alpha'$	$[\bar{1}\bar{1}0]\|\|[\bar{1}1\bar{1}]$	[-0.4583 0.5683 0.6834]	50.75
V11		$[011]\|\|[\bar{1}\bar{1}1]$	[-0.5156 0.0586 0.8548]	13.41
V12		$[011]\|\|[\bar{1}1\bar{1}]$	[-0.6602 0.1887 0.7270]	57.34
V13		$[0\bar{1}1]\|\|[\bar{1}\bar{1}1]$	[-0.0586 0.5156 0.8548]	13.41
V14		$[0\bar{1}1]\|\|[\bar{1}1\bar{1}]$	[-0.5683 0.4583 0.6834]	50.75
V15	$(\bar{1}11)\gamma$	$[\bar{1}0\bar{1}]\|\|[\bar{1}\bar{1}1]$	[-0.2407 0.6666 0.7055]	56.03
V16	$\|\|(011)\alpha'$	$[\bar{1}0\bar{1}]\|\|[\bar{1}1\bar{1}]$	[-0.6907 0.2142 0.6907]	16.37
V17		$[110]\|\|[\bar{1}\bar{1}1]$	[-0.6480 0.4001 0.6480]	50.91
V18		$[110]\|\|[\bar{1}1\bar{1}]$	[-0.2694 0.6593 0.7019]	51.11
V19		$[\bar{1}10]\|\|[\bar{1}\bar{1}1]$	[-0.2092 0.6560 0.7252]	52.30
V20		$[\bar{1}10]\|\|[\bar{1}1\bar{1}]$	[-0.1887 0.6602 0.7270]	57.34
V21	$(11\bar{1})\gamma$	$[0\bar{1}\bar{1}]\|\|[\bar{1}\bar{1}1]$	[-0.1313 0.0000 0.9913]	18.69
V22	$\|\|(011)\alpha'$	$[0\bar{1}\bar{1}]\|\|[\bar{1}1\bar{1}]$	[-0.6593 0.2694 0.7019]	51.11
V23		$[101]\|\|[\bar{1}\bar{1}1]$	[-0.6666 0.2407 0.7055]	56.03
V24		$[101]\|\|[\bar{1}1\bar{1}]$	[-0.2403 0.0000 0.9707]	18.98
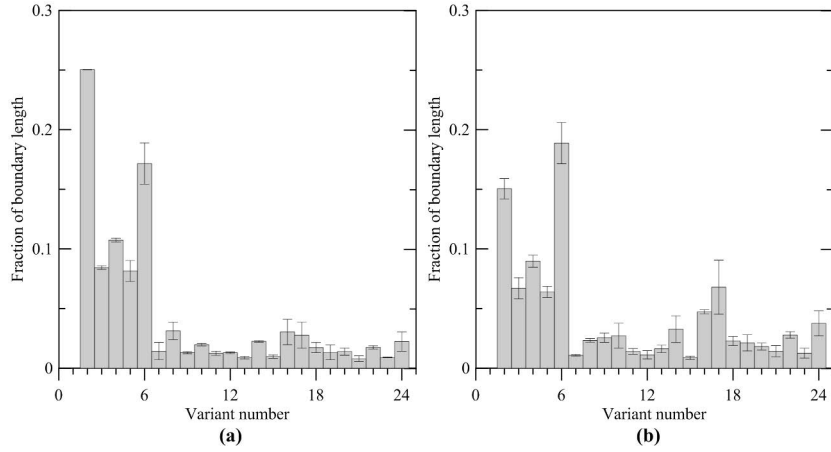
Figure 9: Intervariant boundary histograms for a) Steel A, $T_{iq} = 125°C, t_P = 100s$ and b) Steel B, $T_{iq} = 100°C, t_P = 100s$.

The fraction of each intervariant boundary type from total intervariant boundary length was calculated and is presented as a histogram in Figure 9. The error bars represent the standard deviation between results from the three orientation maps. The most prevalent variant pairing in either steel was the twin boundary V1-V2, corresponding to an approximately 60° misorientation around the $(1\bar{1}1)$ axis and V1-V6, which describes an approximately 50° rotation around $(0\bar{1}\bar{1})$.

Part of the resolved structure is presented in Figure 10. In the Figure, retained austenite is shown with white boundaries, along with packet boundaries within the martensite. Further, in order to better visualize variant distribution, each martensite orientation visualized in the Figure has been assigned a variant number based on the approximate parallelism of close-packed planes and orientations between the martensite orientation pixel and corresponding retained austenite. Again, the notation by Morito et al. [23] is followed in the Figure, so that the variant groups V1-V6, V7-V12, V13-V18 and V19-V24 each correspond to a packet sharing the same set of nearly parallel close-packed $\{111\}\gamma$-
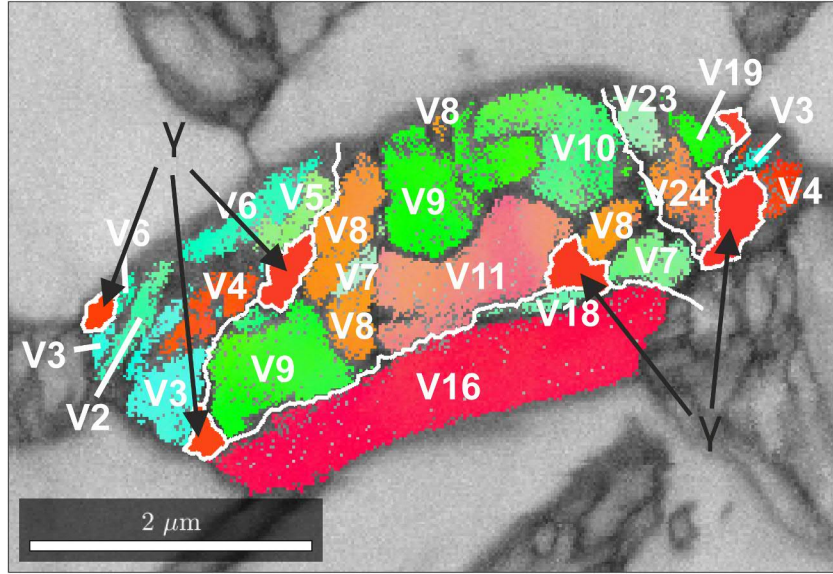
24

Figure 10: Band contrast EBSD map of Steel A quenched to 125 °C and partitioned for 100 s. The map is overlaid with the IPF ND colored orientation map of martensite and retained austenite originating from the same prior austenite grain. Retained austenite and packet boundaries are colored white. The numbers indicate the variant number of the martensite as per the indexing scheme proposed by Morito et al. [23]. Regarding references to color, see the online version of the article.

and $\{011\}\alpha'$-type planes (see Table 3). The variant numbering clearly follows the packet boundaries determined with the iterative method [16]. The morphology of the martensitic blocks deviates slightly from a strict V1-V4 block configuration typical for low-carbon martensite [23, 24]: instead of blocks, the most common substructural martensitic unit appears to be a packet composed of single martensitic variants. The observations made for Figure 10 are supported by the histogram in Figure 9, which shows a relatively small fraction of V1-V4 type sub-block boundaries for both Steels.

The morphology and crystallography of the martensite follows earlier observations for high-carbon lath martensite [23, 24]. Morito et al. [23] attributed the tendency towards single-variant blocks to a greater need (compared to low-

carbon lath martensite) for plastic self-accommodation resulting from high carbon content and (consequent) low transformation temperature. Stormvinter et al. [24] made similar observations, also noting an increased tendency towards twin type lath pairing between V1-V2 type variants. The formation of this type of twinned lath structure has been shown to coincide with low transformation temperatures in the case of martensite [24], bainite [25] and isothermal martensite [26].

After intercritical annealing, the carbon content of the intercritical austenite phase corresponds to high-carbon austenite, as evidenced by the low M_s values and low intercritical austenite fractions observed in a previous study [13]. This explains the observed variant structure corresponding to high-carbon martensite. The notable difference in the structures observed here is the increased fraction of V1-V6 type boundaries in the martensite. The previous studies [24, 25, 26] concern fully austenitized microstructures, in which the prior austenite grain size is an order of magnitude [25, 26] or several orders of magnitude [24] higher than in the intercritically annealed microstructure studied in this work. The small size of the austenite will likely increase the need for self-accommodation of new martensite. Okamoto et al. [27] reported that the V1-V6 variant pairing in thin-plate martensite formed in a Fe-Ni-C alloy provided self-accommodation for the new plate, based on the calculated total shape strain of this variant combination. Morito et al. [23] have calculated a similar result for V1-V6 for low- and high-carbon steels. It is possible that after an initial formation of V1-V2 type variants, the further progression of the martensitic transformation will happen through the formation of a self-accommodating variant in the neighborhood of this combination.

It is probable that some austenite on the analyzed surface has transformed during specimen preparation and the resolution limitations of EBSD make it difficult to observe film-like nanoscale austenite. As shown by Figure 10, the retained austenite observed in the EBSD studies here resided at prior austenite and packet boundaries. These sites are likely to increase the stability of the retained austenite, owing to the difficulties in providing plastic self-accommodation due to the presence of multiple neighboring cross-packet variants or an incoherent prior austenite grain boundary.

6. Conclusions

1. It was shown that it was possible to obtain carbon-stabilized retained austenite by quenching and partitioning in an intercritically annealed microstructure in a high-aluminum steel, with the amount of retained austenite correlating with T_{iq}.

2. The steels exhibited high degrees of work hardening and good ductility, with both Ag and ε_{tot} correlating with the amount of retained austenite.

3. The degree of martensitic transformation was shown to vary from grain to grain. This behavior was rationalized on the basis of grain size and chemical inhomogenuity.

4. The formed martensite has a single-variant block structure and a tendency towards the formation of V1-V2 and V1-V6 type variant combinations. This was justified by the need to form self-accommodating variants (V1-V6) after the initial formation of variant pairs with a high degree of shape strain (V1-V2).

27

5. Highly stable retained austenite was found to reside almost exclusively at prior austenite and packet boundaries.

7. Acknowledgements

8. Data availability

The raw EBSD (DOI: 10.17632/y3knj7x2bx.1), XRD and tensile test data required to reproduce these findings are available to download from `https://data.mendeley.com/datasets/th8bgn6cy8/1` and `https://data.mendeley.com/datasets/y3knj7x2bx/1`. The processed EBSD (DOI: 10.17632/y3knj7x2bx.1), XRD and tensile test data required to reproduce these findings are available to download from `https://data.mendeley.com/datasets/r536xfm8yc/1` and `https://data.mendeley.com/datasets/y3knj7x2bx/1`.

The raw/processed Mössbauer data required to reproduce these findings cannot be shared at this time due to technical or time limitations.

The calculations (DOI: 10.17632/d889hnyk2f.1) required to reproduce Figure 1 are available to download from `https://data.mendeley.com/datasets/d889hnyk2f/1`.

28

9. References

[1] J. G. Speer, F. C. R. Assunção, D. K. Matlock, D. V. Edmonds, The "quenching and partitioning" process: background and recent progress, Materials Research 8 (2005) 417–423.

[2] J. Maki, J. Mahieu, B. De Cooman, S. Claessens, Galvanisability of silicon free CMnAl TRIP steels, Materials Science and Technology 19 (2003) 125–131.

[3] J. G. Speer, D. K. Matlock, B. C. De Cooman, J. G. Schroth, Carbon partitioning into austenite after martensite transformation, Acta Materialia 51 (2003) 2611–2622.

[4] N. Saunders, U. K. Z. Guo, X. Li, A. P. Miodownik, J. P. Schillé, Using JMatPro to model materials properties and behavior, JOM 55 (2003) 60–65.

[5] H. K. D. H. Bhadeshia, Driving force for martensitic transformation in steels, Metal Science 15 (1981) 175–177.

[6] H. K. D. H. Bhadeshia, Thermodynamic extrapolation and martensite-start temperature of substitutionally alloyed steels, Metal Science 15 (1981) 178–180.

[7] S. Van Bohemen, J. Sietsma, Martensite Formation in Partially and Fully Austenitic Plain Carbon Steels, Metallurgical and Materials Transactions A 40 (2009) 1059–1068.

[8] S. M. van Bohemen, J. Sietsma, Effect of composition on kinetics of athermal martensite formation in plain carbon steels, Materials Science and Technology 25 (2009) 1009–1012.

29

[9] C. I. Garcia, A. J. Deardo, Formation of austenite in 1.5 pct Mn steels, Metallurgical Transactions A 12 (1981) 521–530.

[10] G. R. Speich, V. A. Demarest, R. L. Miller, Formation of austenite during intercritical annealing of dual-phase steels, Metallurgical and Materials Transactions A 12 (1981) 1419–1428.

[11] E. Navara, R. Harrysson, On the mechanism of austenite formation during inter- and subcritical annealing of a C-Mn steel, Scripta Metallurgica 18 (1984) 605 – 610.

[12] D. San Martín, Y. Palizdar, C. García-Mateo, R. C. Cochrane, R. Brydson, A. J. Scott, Influence of aluminum alloying and heating rate on austenite formation in low carbon-manganese steels, Metallurgical and Materials Transactions A 42 (2011) 2591–2608.

[13] T. Nyyssönen, P. Peura, V.-T. Kuokkala, Crystallography, morphology, and martensite transformation of prior austenite in intercritically annealed high-aluminum steel, Metallurgical and Materials Transactions A 49 (2018) 6426–6441.

[14] H. Yang, H. Bhadeshia, Austenite grain size and the martensite-start temperature, Scripta Materialia 60 (2009) 493–495.

[15] E. Jimenez-Melero, N. van Dijk, L. Zhao, J. Sietsma, S. Offerman, J. Wright, S. van der Zwaag, The effect of aluminium and phosphorus on the stability of individual austenite grains in TRIP steels, Acta Materialia 57 (2009) 533–543.

[16] T. Nyyssönen, M. Isakov, P. Peura, V.-T. Kuokkala, Iterative determination of the orientation relationship between austenite and martensite from

a large amount of grain pair misorientations, Metall. Mater. Trans. A 47 (2016) 2587–2590.

[17] ASTM E975 - 13 Standard Practice for X Ray Determination of Retained Austenite in Steel with Near Random Crystallographic Orientation (2013).

[18] D. Pierce, D. Coughlin, D. Williamson, K. Clarke, A. Clarke, J. Speer, E. De Moor, Characterization of transition carbides in quench and partitioned steel microstructures by Mössbauer spectroscopy and complementary techniques, Acta Materialia 90 (2015) 417–430.

[19] ISO 2566-1:1984(E) Steel – Conversion of elongation values – Part 1: Carbon and low alloy steels, 1984.

[20] D. Pierce, D. Coughlin, K. Clarke, E. D. Moor, J. Poplawsky, D. Williamson, B. Mazumder, J. Speer, A. Hood, A. Clarke, Microstructural evolution during quenching and partitioning of 0.2C-1.5Mn-1.3Si steels with Cr or Ni additions, Acta Materialia 151 (2018) 454 – 469.

[21] M. Calcagnotto, Y. Adachi, D. Ponge, D. Raabe, Deformation and fracture mechanisms in fine- and ultrafine-grained ferrite/martensite dual-phase steels and the effect of aging, Acta Materialia 59 (2011) 658 – 670.

[22] G. Kurdjumov, Journal of the Iron and Steel Institute 195 (1960) 26.

[23] S. Morito, H. Tanaka, R. Konishi, T. Furuhara, T. Maki, The morphology and crystallography of lath martensite in Fe-C alloys, Acta Materialia 51 (2003) 1789–1799.

[24] A. Stormvinter, G. , T. Furuhara, P. Hedström, A. Borgenstam, Effect of carbon content on variant pairing of martensite in FeC alloys, Acta Materialia 60 (2012) 7265–7274.

[25] N. Takayama, G. Miyamoto, T. Furuhara, Effects of transformation temperature on variant pairing of bainitic ferrite in low carbon steel, Acta Materialia 60 (2012) 2387 – 2396.

[26] R. Naraghi, P. Hedström, A. Borgenstam, Spontaneous and deformation-induced martensite in austenitic stainless steels with different stability, Steel Research International 82 (2011) 337–345.

[27] H. Okamoto, M. Oka, I. Tamura, Couplings of Thin-plate Martensites in an Fe-Ni-C Alloy, Transactions of the Japan Institute of Metals 19 (1978) 674–684.